ARTICLES
https://doi.org/10.1038/s41551-019-0435-y

nature biomedical engineering

Bioresorbable photonic devices for the spectroscopic characterization of physiological status and neural activity

Wubin Bai[1,2,20], Jiho Shin[3,20], Ruxing Fu[4,20], Irawati Kandela[5,6], Di Lu[1,2], Xiaoyue Ni[1,2], Yoonseok Park[1,2], Zhonghe Liu[7], Tao Hang[8], Di Wu[2,9], Yonghao Liu[7], Chad R. Haney[6,10], Iwona Stepien[5,6], Quansan Yang[2,11], Jie Zhao[1,2], Khizar Rehan Nandoliya[12], Hao Zhang[1,2,13], Xing Sheng[14], Lan Yin[4], Keith MacRenaris[6,10], Anlil Brikha[6,10], Fraser Aird[5,6], Maryam Pezhouh[15], Jessica Hornick[16], Weidong Zhou[7] and John A. Rogers[1,2,9,11,12,17,18,19]*

Capabilities in real-time monitoring of internal physiological processes could inform pharmacological drug-delivery schedules, surgical intervention procedures and the management of recovery and rehabilitation. Current methods rely on external imaging techniques or implantable sensors, without the ability to provide continuous information over clinically relevant timescales, and/or with requirements in surgical procedures with associated costs and risks. Here, we describe injectable classes of photonic devices, made entirely of materials that naturally resorb and undergo clearance from the body after a controlled operational lifetime, for the spectroscopic characterization of targeted tissues and biofluids. As an example application, we show that the devices can be used for the continuous monitoring of cerebral temperature, oxygenation and neural activity in freely moving mice. These types of devices should prove useful in fundamental studies of disease pathology, in neuroscience research, in surgical procedures and in monitoring of recovery from injury or illness.

Understanding metabolic and physiological pathways associated with critical diseases is essential in providing target-specific, timely and effective therapeutic treatments[1–3]. Measurements of local changes in these pathways can serve as the basis for optimized pharmacological delivery schedules, surgical intervention procedures and recovery/rehabilitation protocols[4–6]. Functional magnetic resonance imaging, near-infrared spectroscopy, magnetoencephalography and positron emission tomography techniques offer powerful capabilities for monitoring internal body processes in such contexts, but they cannot provide continuous measurements over timeframes that can range from days to months or more. Traditional electronic implants can be considered, but they require subsequent surgical extraction to eliminate unnecessary device loads on (and associated health risks to) the patient[7–9].

In comparison, bioresorbable electronic technologies offer unique opportunities whereby diagnosis and therapy can occur continuously at targeted depths inside the body for well-defined, finite time periods matched to those of the treatment and recovery processes. Complete bioresorption into benign end products that clear through natural body mechanisms eliminates the hardware without the need for secondary surgeries[10–16]. Recent examples include: bioresorbable electronic sensors to track intracranial pressure[11] and to spatiotemporally map electrical activity from the cerebral cortex and cardiac muscle tissue[17,18]; devices to apply controlled therapy for endovascular diseases[19]; and platforms to affect infection abatement[12]. As a complement to electronic sensing modalities, spectroscopic measurements at visible and near-infrared wavelengths can reveal physical and chemical properties of biological tissues, thereby providing a strategy for monitoring vital biochemical processes and sensing key physiological parameters[20–23]. Here, we report materials, device architectures, performance attributes, biocompatibility assessments and in vivo demonstrations of multifunctional bioresorbable devices for spectral characterization of biotissues and biofluids. The presented designs allow for minimally invasive implantation via an injection process, with a construction in which all constituent materials naturally resorb via hydrolysis followed by metabolic clearance after a well-defined operational time. The technology enables continuous monitoring of critical

[1]Department of Materials Science and Engineering, Northwestern University, Evanston, IL, USA. [2]Center for Bio-Integrated Electronics, Northwestern University, Evanston, IL, USA. [3]Department of Chemical and Biomolecular Engineering, University of Illinois Urbana–Champaign, Urbana, IL, USA. [4]School of Materials Science and Engineering, Tsinghua University, Beijing, China. [5]Center for Developmental Therapeutics, Northwestern University, Evanston, IL, USA. [6]Chemistry Life Processes Institute, Northwestern University, Evanston, IL, USA. [7]Department of Electrical Engineering, University of Texas at Arlington, Arlington, TX, USA. [8]State Key Laboratory of Metal Matrix Composites, School of Materials Science and Engineering, Shanghai Jiao Tong University, Shanghai, China. [9]Department of Biomedical Engineering, Northwestern University, Evanston, IL, USA. [10]Center For Advanced Molecular Imaging, Northwestern University, Evanston, IL, USA. [11]Department of Mechanical Engineering, Northwestern University, Evanston, IL, USA. [12]Department of Chemistry, Northwestern University, Evanston, IL, USA. [13]Department of Chemistry, Key Laboratory of Bioorganic Phosphorus Chemistry & Chemical Biology, Tsinghua University, Beijing, China. [14]Department of Electronic Engineering, Tsinghua University, Beijing, China. [15]Northwestern Medicine, Feinberg School of Medicine, Northwestern University, Evanston, IL, USA. [16]Biological Imaging Facility, Northwestern University, Evanston, IL, USA. [17]Department of Neurological Surgery, Northwestern University, Evanston, IL, USA. [18]Department of Electrical and Computer Engineering, Northwestern University, Evanston, IL, USA. [19]Simpson Querrey Institute for BioNanotechnology, Northwestern University, Evanston, IL, USA. [20]These authors contributed equally: Wubin Bai, Jiho Shin, Ruxing Fu. *e-mail: jrogers@northwestern.edu

physiological parameters such as tissue oxygenation, temperature and neural activity for local information on tissue health and metabolic activity[24]. The devices incorporate a collection of bioresorbable optical components including: single-junction photodetectors based on nanomembranes of device-grade monocrystalline silicon (Si nanomembranes); foundry-produced tri-colour photodetectors based on tri-layer stacks of Si P–N junctions; optical multilayer filters of SiO_x and SiN_y; and optical fibres of poly(lactic-*co*-glycolic acid) (PLGA). System-level demonstrations include devices that inject into deep brain regions of freely moving mice for continuous absorption spectroscopic analysis of biochemical and physiological status. Systematic in vitro and in vivo studies establish the feasibility and accuracy of the devices in monitoring cerebral oxygenation, neural activity and temperature. Studies of biodistribution, blood chemistry and complete blood count highlight processes by which these technologies undergo bioresorption.

Results and discussion

Configuring the devices into shapes that resemble hypodermic needles, with dimensions around 600 µm wide and 160 µm thick, facilitates minimally invasive implantation (Fig. 1a). The active sensing region (Fig. 1b,c), supported on a substrate of PLGA (thickness: 10 µm), consists of three key components: (1) a bioresorbable fibre (diameter: ~150 µm) made of PLGA (refractive index: ~1.50) for delivering light of a certain wavelength to the sensing probe; (2) a bioresorbable photodetector made from a nanomembrane of doped monocrystalline Si (thickness: 1,500 nm) for generating electrical signals in response to transmitted light; and (3) electrodes made of thin films of zinc (Zn) (thickness: 400 nm) for electrical readout. A thin layer of SiO_2 (thickness: ~50 nm; refractive index: ~1.45; Fig. 1b) separates the PLGA fibre from the substrate to enhance light confinement inside the fibre, and to encapsulate, for a controlled period of time[25], the electrical components (photodetectors and Zn electrodes). The photodetector uses comb-like geometries (Fig. 1d) for both *p*- and *n*-doped regions to maximize the area coverage of the depletion region and to enhance the overall quantum efficiency (Supplementary Table 1). The measured current–voltage (*I*–*V*) curves in the dark and during illumination with green (wavelength: 530 nm), red (wavelength: 633 nm) and white light (broad-band wavelength) show excellent rectifying behaviour (Fig. 1e), with a dark current of 4.97×10^{-2} nA, responsivities of 0.135 and 0.133 A W^{-1} for green and red light, respectively, and quantum efficiencies of 31.5 and 26% for light at these wavelengths, respectively (Supplementary Table 1). The photocurrent density exhibits a linear response with optical power density, examined at red (633 nm) and near-infrared (850 nm) wavelengths (Fig. 1f). The photocurrent as a function of time under time-modulated illumination (rectangular temporal waveform, using light at a wavelength of 633 nm; Fig. 1h) shows response times of <0.1 s with no observable overshoot or oscillation.

Another key component—the biodegradable fibre—results from a simple drawing process applied to a bulk preform heated to 200 °C on a hotplate to yield a PLGA core (Supplementary Fig. 1a)[26]. Using the tip of a commercial fibre as a lead for the fibre-drawing process directly couples the resulting bioresorbable fibre to the commercial fibre (Supplementary Fig. 18). Dipping into sodium alginate solution (2 wt%) forms a uniform coating of a bioresorbable hydrogel (alginate) that serves as a cladding (Supplementary Fig. 1a). Immersion into a calcium chloride solution (0.5 wt%) ionically crosslinks the alginate to complete the fabrication (Supplementary Fig. 1 and Supplementary Note I show that the optically improved performance can be achieved using multiple cladding layers, which include a 200-nm-thick sputtered SiO_2 and alginate hydrogel (Supplementary Fig. 19)). Connecting the bioresorbable optical probe through a commercial fibre (diameter: 1 mm) to an external tunable laser source (an NKT Photonics SuperK COMPACT supercontinuum laser coupled with a SuperK VARIA tunable single-line filter; tuning range wavelength: 400–840 nm; wavelength accuracy: ±5 nm), and through two wires (diameter: 80 µm), to an external data acquisition system prepares the system for implantation and operation, with little constraint on the freedom of movement during continuous physiological monitoring in awake animal models (Supplementary Figs. 2 and 13).

An essential feature of the implanted components is that the constituent materials (Si, Zn, SiO_2 and PLGA) are entirely bioresorbable by dissolution reactions in biofluids to yield benign end products including H_4SiO_4, $Zn(OH)_2$, lactide and glycolide, which can be further metabolized and cleared by the body[25,27–30]. Figure 1h,i and Supplementary Fig. 3 characterize the dissolution behaviour of the key components (bioresorbable photodetector and bioresorbable fibre) individually, both in vitro and in vivo. Figure 1h and Supplementary Fig. 3a,b show the measured *I*–*V* curves in the dark and during illumination with white light, and the corresponding optical images of a bioresorbable photodetector at various stages after immersion in phosphate buffered saline (PBS) at 37 °C. The thin SiO_2 encapsulation layer effectively prevents water from penetrating into the active sensing area for the first 2 d. Slopes of these curves gradually decrease with time in forward bias mode, mostly due to hydrolysis of the Si nanomembrane and the Zn electrodes. On day 9, dissolution-induced fracture of the Zn electrodes creates an electrical open that leads to zero measurable photocurrent (Fig. 1h and Supplementary Fig. 3a,b). Immersion of a film of Zn (thickness 1 µm, deposited by electron beam evaporation) in a reservoir of PBS (with a replacement rate of 10 vol.% d^{-1}) at 37 °C reveals that the hydrolysis process leads to fragmentation that yields platelets composed mainly of $Zn(OH)_2$, with some amount of ZnO and Zn, as observed on day 3 (platelet lateral dimensions: ~75–150 µm; Supplementary Fig. 4). The sizes of these platelets decrease with time to dimensions of ~250 nm on day 10. The computed X-ray tomography images in Fig. 1i show the gradual disappearance of an array of bioresorbable photodetectors (the layout appears in Supplementary Fig. 5) implanted in the subcutaneous region near the flank of a mouse model. On day 45, the array is invisible under computed tomography, consistent with complete bioresorption (Fig. 1i). Supplementary Fig. 3c,d shows the dissolution behaviour of the PLGA fibre, indicating an initial swelling on day 1 and a gradual dissolution within 2 weeks in PBS at 37 °C. The optical transmission decreases dramatically on day 3 and eventually become undetectable on day 20.

Basic capabilities in spectroscopic characterization[31] can be realized using a tri-colour bioresorbable Si photodetector (Fig. 2) or a set of bioresorbable optical filters (Fig. 3). Figure 2a presents a schematic (with an exploded view on the right) of the former type of device, which consists of four doped layers (from top to bottom: layers A, B, C and D correspond to *n*-, *p*-, *n*- and *p*-doped layers, respectively, with the doping concentrations and thicknesses shown in Supplementary Table 2) vertically aligned together to form three junctions: AB, BC and CD, respectively[32]. Perspective images (Fig. 2b) generated by optical profilometry and tilted-view scanning electron microscope (SEM) images (Supplementary Fig. 6a,b) highlight the results of etching steps to expose each doped layer (layers A, B, C and D) for metal contacts (as shown in Supplementary Fig. 6c). Coupling this tri-colour photodetector to a PLGA fibre for light delivery and four Zn metal electrodes for electric readout yields a simple, bioresorbable spectrometer (Fig. 2c). Figure 2d shows *I*–*V* curves (in a dark environment) for junctions AB, BC and CD, respectively, indicating excellent rectifying behaviours, with dark currents of 3.24×10^{-2}, 1.52×10^{-1} and 9.87×10^{-3} µA, respectively, and responsivities of 0.15, 0.15 and 0.11, respectively (the measured *I*–*V* curves for junctions AC, BD and AD appear in Supplementary Fig. 6d). The penetration depth of light (wavelengths between 400 and 1,000 nm) in Si increases with wavelength, thereby enabling peak responsivities for junctions AB, BC and CD at wavelengths of 490, 570 and 720 nm, respectively (Fig. 2e). Figure 2f

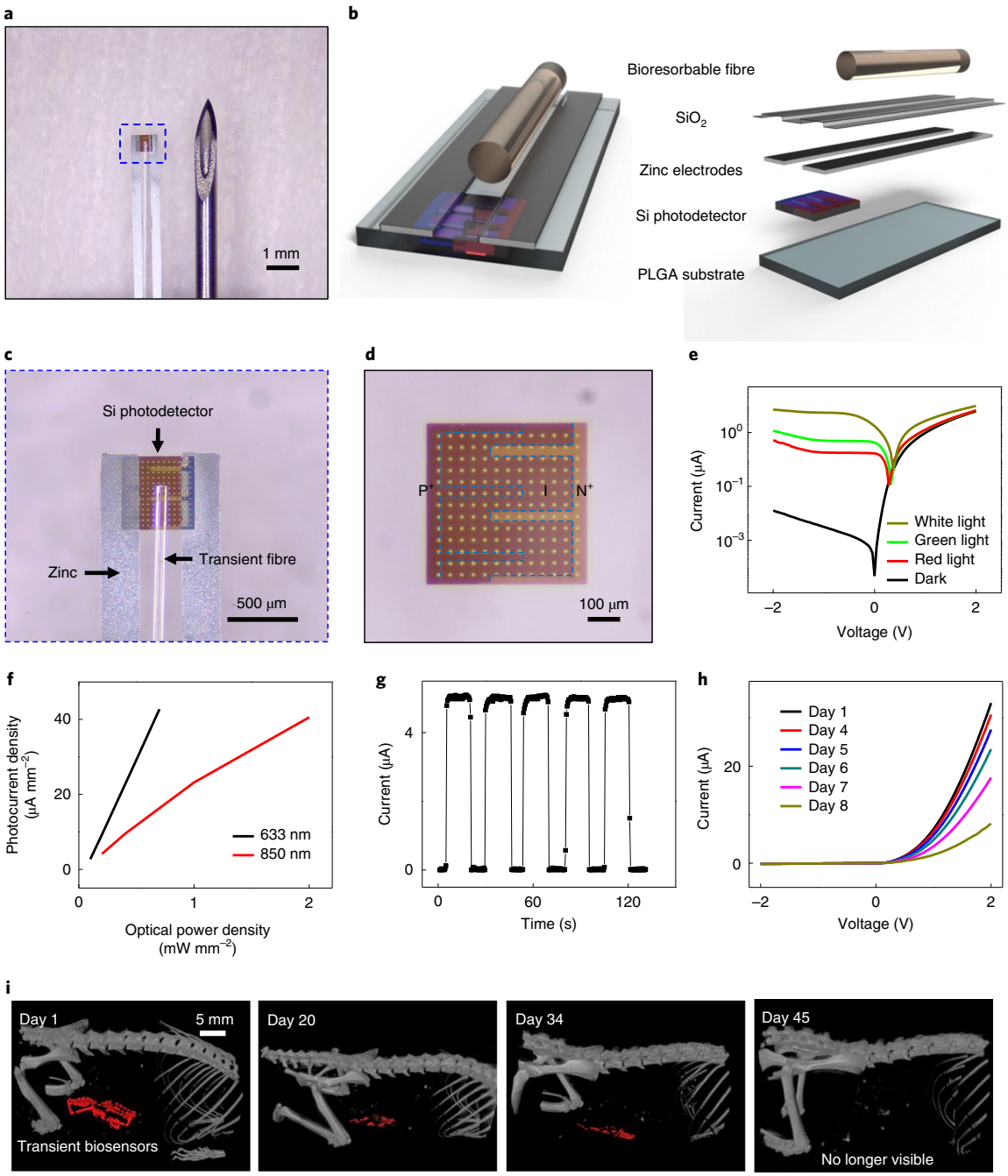

Fig. 1 | Bioresorbable Si photodetector with a bioresorbable fibre optic probe for spectroscopic characterization of biological tissues. a, Optical microscope image of a bioresorbable spectrometer based on an Si nanomembrane photodetector and a bioresorbable fibre optic probe, placed next to the tip of a hypodermic needle (diameter: 650 μm). The device consists of: a photodetector constructed from a 1,500-nm-thick Si nanomembrane; two Zn electrodes (thickness: 400 nm; width: 200 μm); a bioresorbable optical fibre (made from PLGA; diameter: 150 μm); and a supporting substrate made from PLGA (thickness: 10 μm). **b**, Schematic of the device, with an exploded view shown to the right. **c**, Enlarged view of the active sensing region. **d**, Optical image of a fully bioresorbable PIN photodetector constructed with a 1,500-nm-thick Si nanomembrane. Dashed blue lines define the *n*-type, *p*-type and intrinsic regions. **e**, Measured *I*–*V* characteristics of the device under illumination with white light (broad-band wavelength), red light (wavelength: 633 nm) and green light (wavelength: 530 nm), and in a dark environment. **f**, Measured photocurrent density as a function of optical power density for illumination with red (wavelength: 633 nm) and near-infrared light (wavelength: 850 nm). **g**, Measured photocurrent as a function of time for illumination with light after passing through a chopper (red light, wavelength: 633 nm; optical power: 4 mW). **h**, Measured *I*–*V* characteristics (in a dark environment) at various times after immersion in PBS at 37 °C. **i**, Three-dimensional-rendered computed tomography images of mice collected over 7 weeks after the implantation of arrays of bioresorbable Si nanomembrane photodetectors (as shown in Supplementary Fig. 4). The images indicate the gradual disappearance of the devices, which eventually became invisible under computed tomography on day 45. In **e**–**h**, $n = 6$ independent experiments. In **i**, $n = 3$ biologically independent mice.

shows measured photovoltages generated from junctions AB, BC and CD in response to illumination using white light (broad-band wavelength) after passing through a chopper, indicating a response time for all three junctions that is <0.05 s. As the colour content of the illumination changes, the signals generated from the three junctions change accordingly, in a way that reflects the variations

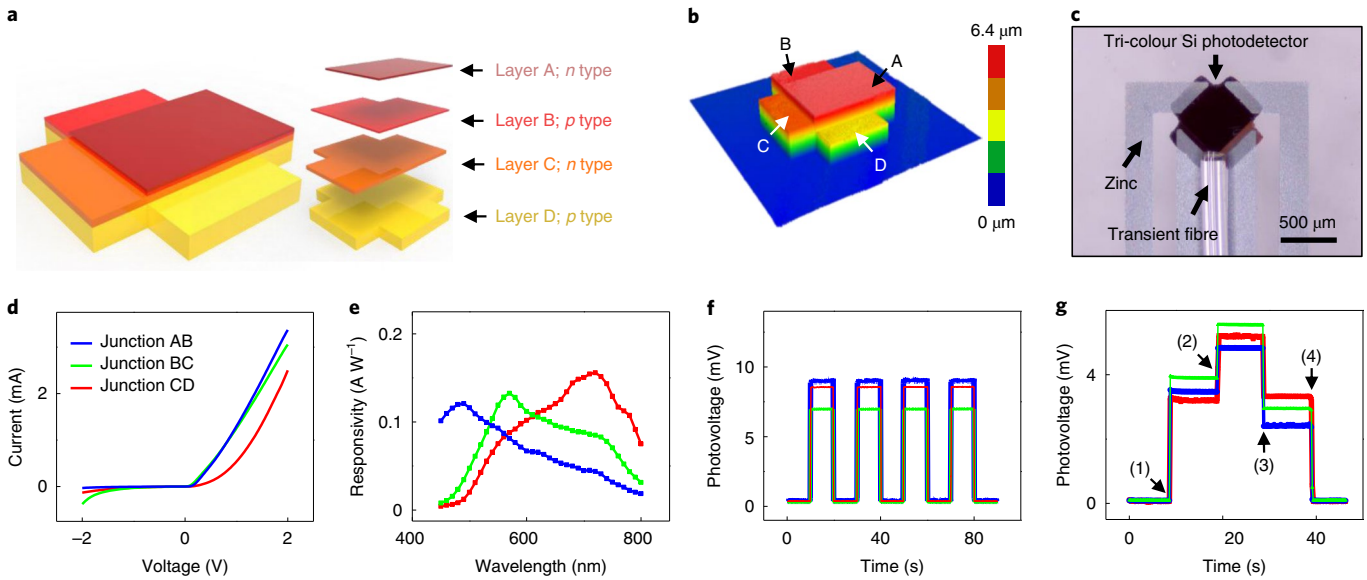

Fig. 2 | Bioresorbable tri-colour Si photodetector with a bioresorbable fibre optic probe for spectroscopic characterization of biological tissues. a, Schematic of a tri-colour Si photodetector, with an exploded view shown on the right. Each pair of adjacent doped layers constitutes a photojunction, with peak sensitivities at 490, 570 and 720 nm for junctions AB, BC and CD, respectively. **b**, Perspective image of the device characterized by an optical profilometer. The labels A, B, C and D indicate contact openings corresponding to layers A, B, C and D, respectively. The colour bar represents quantitative values of height. **c**, Optical microscope image of a bioresorbable spectrometer based on a tri-colour Si photodetector with four Zn electrodes (thickness: 3 μm; width: 200 μm) and a bioresorbable fibre (made from PLGA; diameter: 170 μm). **d**, Measured *I*–*V* characteristics of junction AB (blue line), BC (green line) and CD (red line) in a dark environment. **e**, Measured photoresponses of junctions AB (blue line), BC (green line) and CD (red line) as a function of illumination wavelength. The measured peak wavelengths for junctions AB, BC and CD were 490, 570 and 720 nm, respectively. **f**, Measured photovoltages generated from junction AB (blue line), BC (green line) and CD (red line) as a function of time under illumination with white light (broad-band wavelength) after passing through a chopper. **g**, Measured photovoltages generated from junction AB (blue line), BC (green line) and CD (red line) due to illumination with green and red light in a programmed sequential and combination timer. Arrows highlight the times for changes in illumination ((1) green light on, red light off; (2) green light on, red light on; (3) green light off, red light on; and (4) green light off, red light off. In **d**–**g**, $n = 6$ independent experiments.

in spectral information simultaneously and in real time (Fig. 2g, Supplementary Note VI and Supplementary Fig. 17). Encapsulating the device with a 200-nm-thick SiO_2 layer prepared by sputter deposition enables stable operation for 10 d (Supplementary Note VIII and Supplementary Fig. 21).

Bioresorbable optical filters use multi-stacks of alternating layers of SiO_x and SiN_y with a controlled periodicity or combination of several periodicities (Fig. 3) to modulate the transmission and reflection spectra in a desired manner[33,34]. Transferring such a stack from its growth substrate onto a 10-μm-thick PLGA film and drop casting another 10-μm-thick PLGA film on top locates the filter at the neutral mechanical plane to yield a flexible and fully bioresorbable optical element (Fig. 3a,b) with bending radii that can be as small as 300 μm. As shown in the cross-sectional SEM images (Fig. 3c (80° tilted view) and Supplementary Fig. 7a,b (90° tilted view)), the optical filters used here consist of multiple pairs (3–15 pairs for the examples shown here) of SiO_x and SiN_y films with thicknesses of 54 and 85 nm, respectively. The depth profile of the refractive index corresponding to 15 pairs of SiO_x and SiN_y films appears in Fig. 3d. The result is a band-stop filter with blocking wavelength from 450–520 nm and an optical density around 3.52, consistent with the simulation results (Fig. 3e; Supplementary Fig. 7c reveals that decreasing the number of pairs of SiO_x and SiN_y films decreases the optical density). Measurements of the angular dependence of the transmission spectrum show both a slight shift towards lower wavelength and a narrowing of the width of the stop-band with an increasing angle of incidence, consistent with simulation (Fig. 3f). Controlling the number of pairs of SiO_x and SiN_y films and the thickness of each film enables fabrication of bioresorbable optical filters with various filtering characteristics (Supplementary Fig. 16 and Supplementary Note X). Incorporating such a filter into a bioresorbable spectrometer by integration on the top surface of a photodetector via lamination at 55 °C enables, as an example, the detection of fluorescence-based calcium indicators of neural activity, including GCaMP (a type of genetically encoded fluorescence with an excitation wavelength of ~480 nm and an emission wavelength of ~510 nm) and Oregon Green 488 BAPTA-2 AM (a type of cell-permeable fluorescence with an excitation wavelength of 494 nm and an emission wavelength of 523 nm)[35].

Immersing these types of bioresorbable optical filters in PBS at 37 °C results in a gradual lowering of the optical transmission, mostly due to degradation of the PLGA encapsulation layer (Fig. 3g). Figure 3h provides thickness profiles and atomic force microscopy (AFM) images of pyramidal structures composed of such multilayers at several times after immersion in PBS (pH 7.4) at 80 °C (additional AFM images and thickness profiles at 80 °C and pH 5, achieved by adding acetic acid in PBS, appear in Supplementary Fig. 7). The observations indicate that the rate of dissolution (3 ± 1 nm d^{-1}) and total stress (85 MPa; compressive) of the multilayer structure are smaller than those of the individual material components, deposited under similar conditions, and similar to those for SiO_xN_y (Supplementary Fig. 7d–j). Specifically, the dissolution rates for SiO_x produced by low-frequency plasma-enhanced chemical vapour deposition (PECVD), SiN_y produced by high-frequency PECVD, SiN_y produced by low-frequency PECVD, and SiO_xN_y produced by high-frequency PECVD are 5 ± 3, 12 ± 2, 20 ± 5 and 3 ± 2 nm d^{-1}, respectively (Supplementary Fig. 7d–f,j), with corresponding film stresses of 399 (compressive), 123 (tensile), 748 (compressive) and 37 MPa (compressive), respectively (Supplementary Fig. 7g,h). These observations suggest a correlation between the residual stress and the rate of dissolution[36].

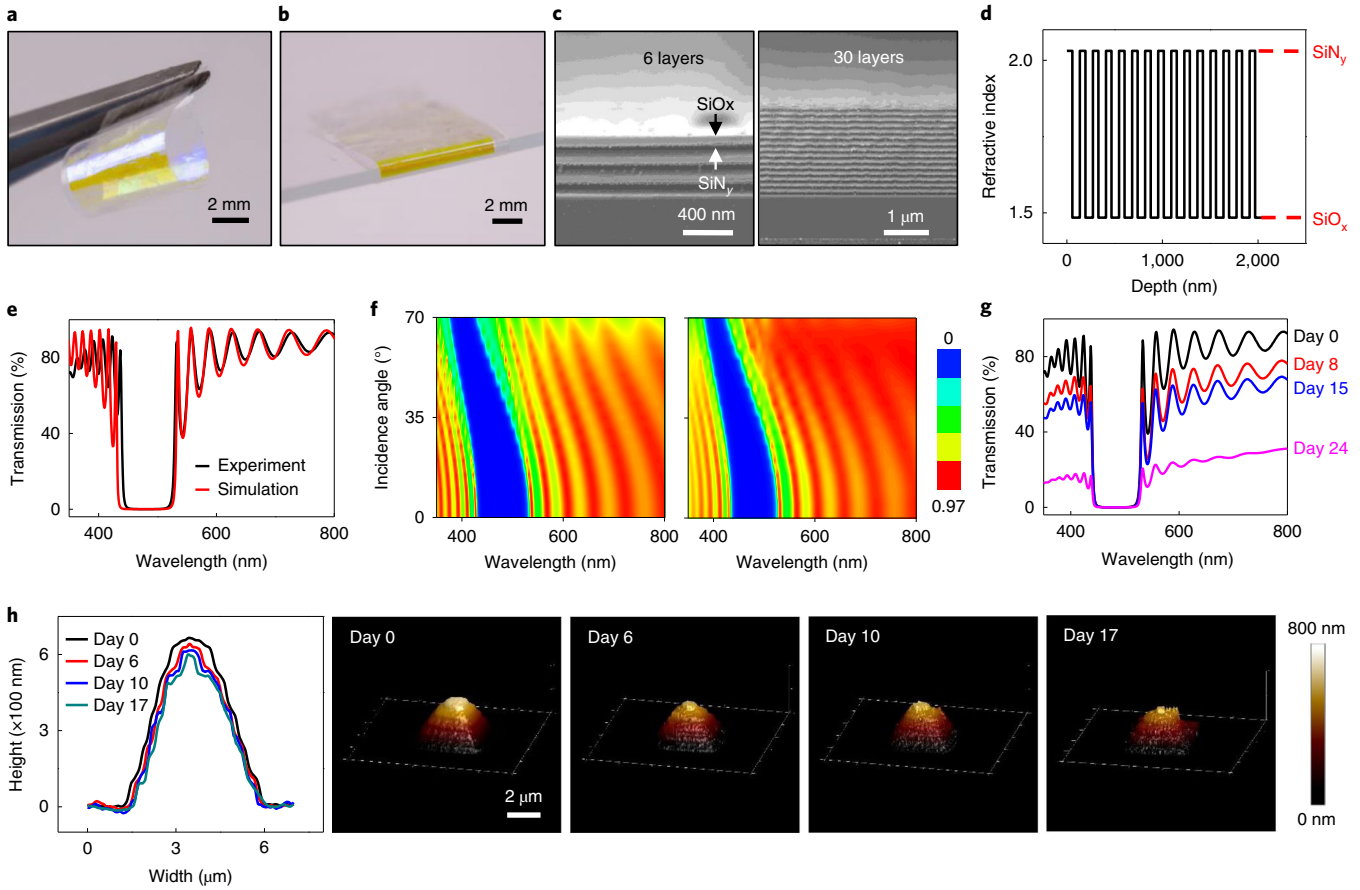

Fig. 3 | Bioresorbable optical filter based on multilayer assemblies of films of SiO_x and SiN_y. **a**, Image of a bioresorbable optical filter that consists of 15 pairs of SiO_x and SiN_y films with thicknesses of 54 and 85 nm, respectively, encapsulated by a film of PLGA with a thickness of 10 μm. **b**, Image of the filter wrapped onto the edge of a glass slide with a thickness of 1 mm. **c**, Cross-sectional SEM images (80° tilted view) of the multilayer stack. The left and right images correspond to 3 and 15 pairs, respectively, of SiO_x and SiN_y films, with total thicknesses of 417 and 2,085 nm, respectively. **d**, Depth profile of the refractive index for a filter with 15 pairs. The refractive indices of SiO_x and SiN_y are 1.48 and 2.03, respectively. **e**, Experimental and simulation results of the transmission spectrum of a filter at a 0° incidence angle. The filter effectively blocks excitation light (peak wavelength: 494 nm) and transmits emission light (peak wavelength: ~523 nm) for a Ca^{2+}-sensitive fluorophore (Oregon Green BAPTA-2 AM). **f**, Simulation (left) and experimental (right) results for transmission spectra of a bioresorbable optical filter at incidence angles between 0 and 70°. The colour bar represents quantitative values of transmission. **g**, Transmission spectra of a filter measured at various times after immersion in PBS at 37 °C. The decrease in transmission mostly arose from degradation of the PLGA substrate. **h**, Profiles (left) and AFM topographical images (right) of a multilayer of SiO_x and SiN_y patterned into a square pad with sloping sidewalls, at various times after immersion in PBS (pH = 7.4) at 80 °C. In **c**–**e**, **f** (right), **g** and **h**, $n = 3$ independent experiments.

Haematology and biochemistry studies of the biodistribution of elements (Si and Zn) associated with dissolution of the biodegradable spectrometers implanted in mouse models reveal the body's reactions to the constituent materials (surgical procedures appear in the Methods). Figure 4a,b shows concentrations of Si (Fig. 4a) and Zn (Fig. 4b) in the blood, brain, heart, kidney, liver, lung, muscle and spleen tissues explanted from mice at 1, 3, 5 and 7 weeks after implantation, measured by inductively coupled plasma optical emission spectrometry (ICP-OES) and inductively coupled plasma mass spectrometry (ICP-MS). The results in all of the measured organs of mice with an implanted device, compared with those in the control group with no implantation, showed no abnormal accumulation of dissolved Si and Zn in the tissues during the 7-week implantation period. Raised concentrations of Si and Zn appeared during the first 3 weeks of study in tissues including the blood, heart, muscle and spleen for Si, and the heart, lung and muscle for Zn, then gradually recovered to within the normal range within 7 weeks. Implantation of a Zn film (thickness 50 μm) in the subcutaneous region near the flank region showed no insoluble flakes/particles generated from the Zn film based on computed tomography (resolution: ~30 μm^3) after 41 d (Supplementary Fig. 4d). The slow increase of concentrations of Si and Zn in the kidneys (from week 1 to week 5 for Si, and from week 1 to week 7 for Zn) suggest renal clearance to maintain the metabolic balance of these materials. Histological analysis of key organ tissues (heart, kidney, lung and spleen) show no damage to the tissue and no identifiable immune cells related to implantation (Fig. 4c). Analysis of complete blood counts and blood chemistry tests also indicate no sign of organ damage or injury, and no change in the electrolyte and enzyme balance (Fig. 4d,e, Supplementary Fig. 8 and Supplementary Note II). Supplementary Fig. 9a,b shows minimal differences in changes in body weight and organ weight associated with implanted mice compared with a control group.

This type of biodegradable spectroscopic technology can be used to measure various physiological parameters that are essential in clinical care and medicine (Fig. 5 and Supplementary Fig. 26 illustrate the experimental setup). Incorporating a tunable laser (such as the NKT Photonics supercontinuum laser coupled with a SuperK VARIA tunable single-line filter) as a light source for the Si nanomembrane-based system yields transmission spectra of blood samples at various oxygenation levels that are consistent with

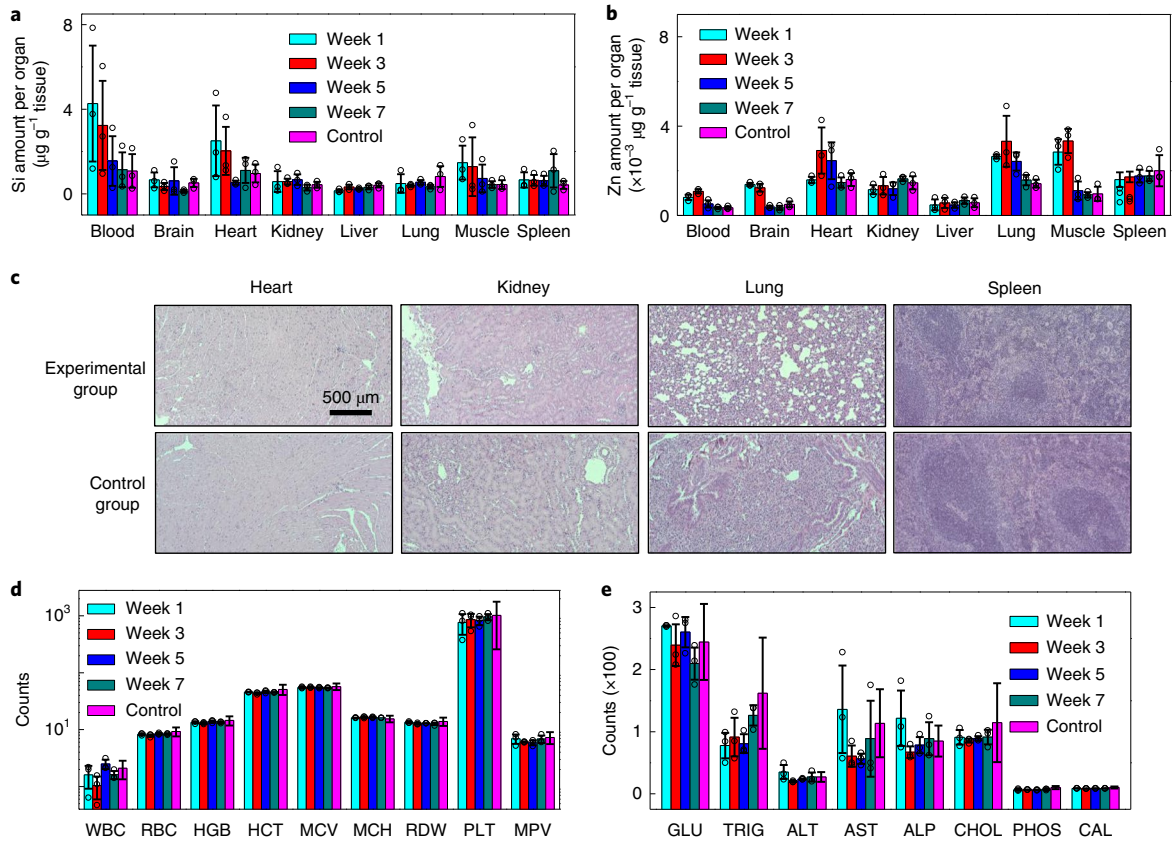

Fig. 4 | In vivo evaluations of elemental biodistribution and biocompatibility of bioresorbable devices for spectroscopic characterization of biological tissues throughout their operational period and beyond. a,**b**, In vivo biodistribution of key elements (Si (**a**) and Zn (**b**)) from bioresorbable devices for spectroscopic characterization of biological tissues. Here, the device consisted of an Si nanomembrane photodetector with the dimensions 500 μm × 500 μm × 1,500 nm (length × width × thickness), two Zn electrodes with the dimensions 2,000 μm × 250 μm × 400 nm, and a PLGA fibre with a diameter 150 μm, as shown in Fig. 1a. Implantation was in the subcutaneous region near the flank region ($n = 12$ biologically independent mice), and comparisons were made with control animals ($n = 3$ biologically independent mice). Euthanizing three experimental mice ($n = 3$ biologically independent mice) at weeks 1, 3, 5 and 7 enabled analysis of the biodistribution and biocompatibility of implanted bioresorbable spectrometers. ICP-OES and ICP-MS defined the concentrations of Si and Zn, respectively, in the blood and organs (brain, heart, kidney, liver, lung, muscle and spleen) explanted at 1, 3, 5 and 7 weeks after implantation. **c**, Histology images of the heart, kidney, lung and spleen of a control mouse and a mouse with a bioresorbable spectrometer implanted for 5 weeks ($n = 6$ independent experiments). **d**,**e**, Analysis of complete blood counts and blood chemistry for the mice in **a** and **b** ($n = 3$ biologically independent mice). Control data were provided by the mouse supplier (Charles River Laboratories). ALP, alkaline phosphatase (IU l^{-1}); ALT, alanine aminotransferase (U l^{-1}); AST, aspartate transaminase (IU l^{-1}); CAL, calcium (mg dl^{-1}); CHOL, cholesterol (mg dl^{-1}); GLU, glucose (mg dl^{-1}); HCT, haematocrit level (%); HGB, blood haemoglobin level (g dl^{-1}); MCH, mean corpuscular haemoglobin (pg); MCV, mean corpuscular volume (fl); MPV, mean platelet volume (fl); PHOS, phosphorus (mg dl^{-1}); PLT, platelet count in blood (×1,000 μl^{-1}); RBC, red blood cell (×1,000,000 μl^{-1}); RDW, red cell distribution width (%); TRIG, triglycerides (mg dl^{-1}); WBC, white blood cell (×1,000 μl^{-1}). In **a**, **b**, **d** and **e**, the results are shown as means ± s.e.m.

expectations (Fig. 5a)[37], with a linear relationship between photocurrent and oxygen saturation across the entire wavelength range (Fig. 5b). Similar strategies can be used to detect other biochemical species, including serum albumin (a common protein in the blood that is essential for stabilizing the extracellular fluid volume; Supplementary Fig. 10) and melanin (a group of natural pigments found in the body that play a critical role in epidemic health, apoptosis and some types of neural disorder; Supplementary Fig. 11 and Fig. 5c,d). Most biomedical applications rely on spectral signatures of associated chemical biomarkers[38–40]. The tri-colour Si photodetector can perform simultaneous detection at three different wavelengths (around 490, 570 and 720 nm; Fig. 5c) when operated with broad-band illumination, thus providing a basic type of continuous spectroscopy (Fig. 5d). Furthermore, the temperature-dependent resistance of the Si nanomembrane photodetector allows for monitoring of tissue temperature at a resolution of ~0.1 °C (Fig. 5e). The addition of a bioresorbable optical filter on the surface of an Si nanomembrane photodetector yields a spectrally selective response that can be aligned, for example, to the fluorescence associated with Ca^{2+} indicators for monitoring neural activity (Fig. 5f and Supplementary Fig. 12)[35]. In vitro tests show a linear relationship (Fig. 5g) between detected signals and Ca^{2+} concentration that is of biological relevance to monitoring neural activity (Fig. 5h).

Deploying these bioresorbable spectrometers in live animal models (Fig. 6 and Supplementary Fig. 14 and 15) shows possibilities for sensing cerebral temperature (Fig. 6e), cerebral oxygen saturation (Fig. 6f,g and Supplementary Fig. 14) and neural activity (Fig. 6h and Supplementary Fig. 15) continuously as the animals move in a cage environment (Fig. 6c). As shown in Fig. 7, implantation of the probes induces minimal inflammatory glial responses (day 1), which then gradually decrease over time to a level comparable to the control group, suggesting normal recovery of the mice from implantation surgery. The viability of the surrounding neurons and glia remained unchanged, compared with that of the control group. The cross-sectional area of the implantation site shows consistent decrease overtime, indicating bioresorption of implanted devices

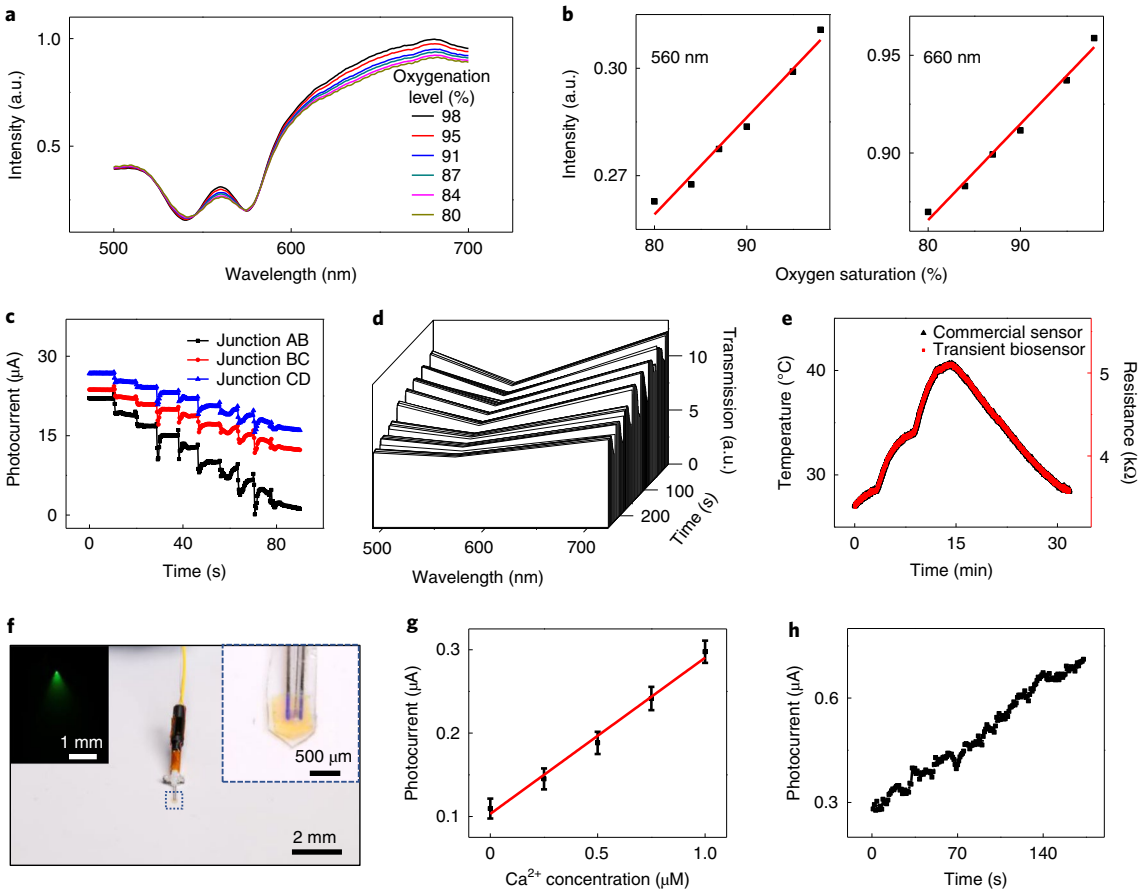

Fig. 5 | In vitro demonstrations of oxygenation, temperature, melanin and Ca^{2+} sensing via spectroscopic measurements using bioresorbable devices. **a**, Spectral response of an Si nanomembrane-based bioresorbable spectrometer to blood with various oxygenation levels. A tuneable laser delivers—through a PLGA fibre into human blood—monochromatic light with wavelengths between 450 and 750 nm. A Si nanomembrane photodetector located at the tip of the fibre generates a photoresponse at each wavelength. **b**, Calibration curves corresponding to responses at wavelengths of 560 nm (left) and 660 nm (right), measured in vitro. **c**, When exposing a bioresorbable tri-colour spectrometer to aqueous surroundings, the measured photocurrent for each junction depends on the optical properties (absorption and/or scattering) of the adjacent materials. The graph shows photocurrents measured from junctions AB, BC and CD from a bioresorbable tri-colour spectrometer during immersion in a PBS solution of melanin with concentrations varying from 0–0.1%. These concentrations are relevant to the typical melanin concentrations of human tissue. **d**, Transmission spectrum based on measurements of the bioresorbable tri-colour spectrometer, in response to melanin solutions of various concentrations from 0% (at $t = 0$ s) to 0.1% (at $t = 248$ s). **e**, Calibrated response of a bioresorbable device (red line), configured as a thermal sensor, compared with a commercial temperature sensor (black line). **f**, Image of a bioresorbable spectrometer that incorporates a bioresorbable optical filter for fluorescence sensing. Left inset: profile of emission light (wavelength: 515 nm) recorded during immersion of the bioresorbable spectrometer in Calcein solution. Excitation light (wavelength: 475 nm) is delivered through the bioresorbable polymer fibre. Right inset: enlarged view of the sensing region of the bioresorbable spectrometer with an integrated filter. The filter bonds on top of the Si nanomembrane photodetector. **g**. In vitro measurements of the bioresorbable spectrometer at various concentrations of calcium (Ca^{2+}) added into Calcein solution. The concentration of Calcein was 5 μM (pH = 13). **h**, In vitro measurements of the bioresorbable spectrometer as calcium solution constantly flowed into the Calcein solution. The concentration of Calcein was 25 μM. The flow rate of Ca^{2+} was 0.25 μM s^{-1}. In **a**–**f** and **h**, $n = 3$ independent experiments. In **g**, $n = 6$ independent experiments. The results are shown as means ± s.e.m.

with no sign of adverse effect on the neighbouring neurons. The morphologies of soma, dendrites and axons of the experimental group (days 1, 7, 14) remain similar to those of the control group (Supplementary Fig. 19), indicating minimal physiological effects on the surrounding neural and glial networks resulting from bioresorbable optical probes. Cerebral temperature reflects metabolic activity and can serve as an indicator of many diseases, such as ischaemic stroke, traumatic brain injury and subarachnoid haemorrhage[41,42]. Fig. 6e highlights such measurements performed on a mouse in the process of taking food after fasting for 5 h. The data indicate a slow increase in temperature starting at ~34.4 °C and eventually reaching ~36.8 °C, with a trajectory consistent with measurements of the skin surface using a thermal camera (Fig. 6e). The overall offset of these two measurements (~0.3 °C on average) is consistent with the expectation that the cerebral temperature should be slightly higher than the epidermal tissue. Thermal images (Fig. 6e (at time (t) = 0, 1.8 and 6.6 min)) collected at various stages of food intake also reveal an increase in body temperature, consistent with the temperature trajectory measured by the implanted device.

Cerebral oxygenation is a diagnostic indicator for various neurological diseases, including hepatic metabolic encephalopathy, meningoencephalitis and intracranial haemorrhage[43–47]. Implanting a bioresorbable spectrometer based on a tri-colour photodetector into the cerebral region near the parietal lobe (Fig. 6d and Supplementary Figs. 13 and 14) and illuminating the system with broad-band light (ranging from 450–750 nm) through the PLGA fibre enables continuous measurements of cerebral oxygenation of freely moving mice. Figure 6f shows measured photocurrents from

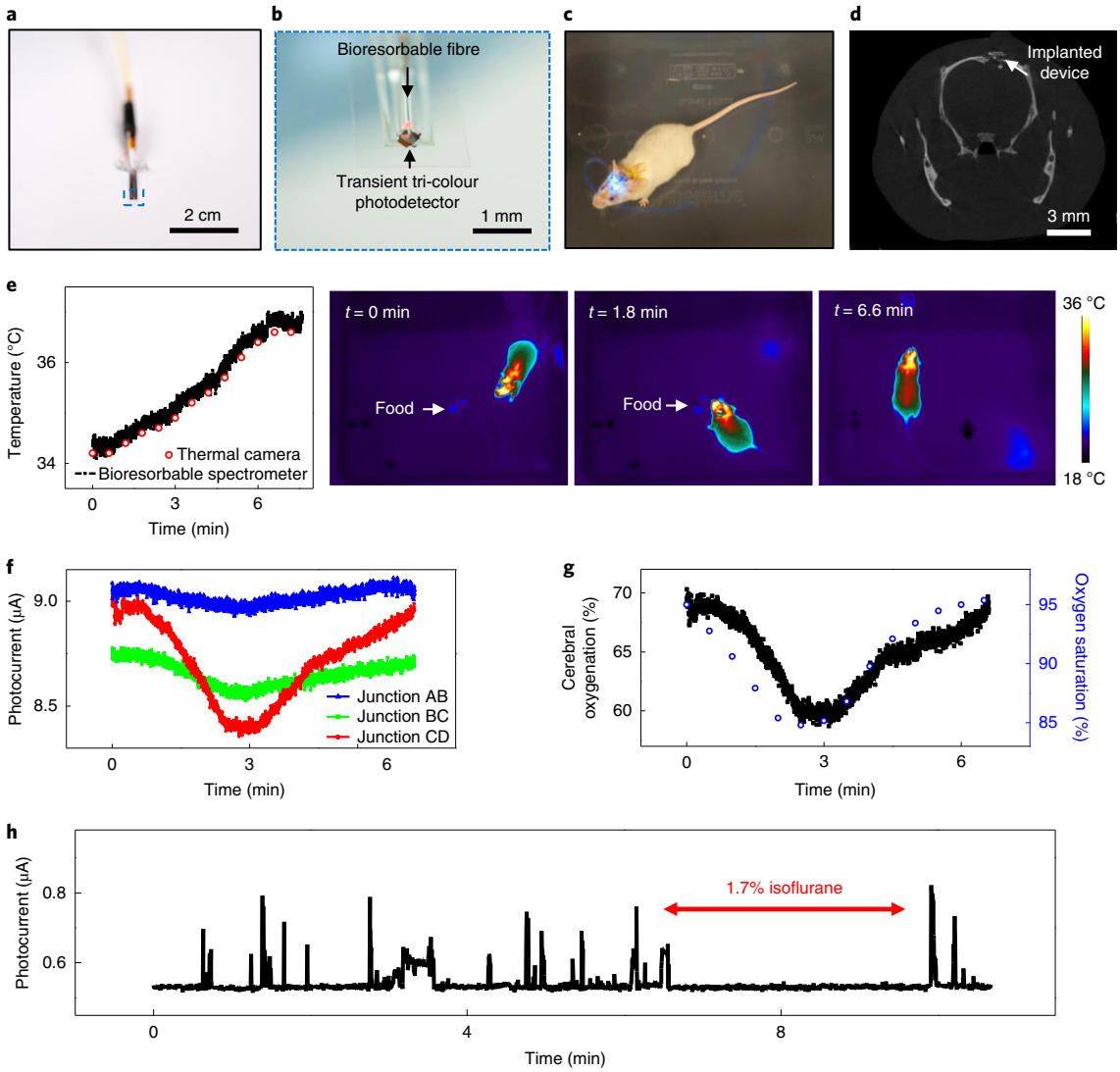

Fig. 6 | Monitoring cerebral temperature, oxygenation and neural activity in freely moving animal models via spectroscopic measurements using bioresorbable devices. a, Image of a bioresorbable spectrometer for surgical implantation into the brain. This device uses a tri-colour Si photodetector. **b**, Enlarged view of the active sensing area of the bioresorbable spectrometer. **c**, Image of a freely moving mouse implanted with a bioresorbable spectrometer. **d**, Axial-view image captured by computed tomography of a mouse implanted with a bioresorbable spectrometer. **e**, Temperature of the brain measured with an implanted bioresorbable spectrometer, and of the surface of the head of the animal using an infrared camera during tests of food intake. The corresponding thermal images (at $t = 0$, 1.8 and 6.6 min) indicate thermal distributions (in the brain and whole body) before, during and after the intake of food. **f**, Measured photocurrents from junctions AB, BC and CD of a tri-colour photodetector-based bioresorbable spectrometer implanted into the cerebral region near the parietal lobe. The environmental oxygen concentration changed from ~20% to ~7% during first 3 min of measurement, and from ~7% back to ~20% during the rest of the measurement. **g**, Cerebral oxygenation calculated based on the measurements of an implanted bioresorbable spectrometer, and blood oxygenation measured by a commercial sensor placed at the hind paw of the mice. **h**, Measured photocurrents from an implanted spectrometer in response to fluorescence (Oregon Green 488 BAPTA-2 AM) modulated by neural calcium transients, illustrating the effects of anaesthetic induction (via 1.7% isoflurane) on neuronal signalling. In **c**–**f** and h, $n = 4$ independent experiments.

junctions AB, BC and CD during changes in the environmental oxygen concentration, indicating that lowering the concentration (from ~20% to ~7%) results in a corresponding increase in light absorption from the brain tissue at wavelengths of ~490, ~570 and ~720 nm, due to the increasing percentage of deoxyhaemoglobin, consistent with a decrease in cerebral oxygenation. Based on the Beer–Lambert law, comparing light absorption measured from junctions BC and CD yields an estimate of cerebral oxygenation (Fig. 6g), consistent with measurements using a commercial oxygenation sensor (PhysioSuite for Mice & Rats; Kent Scientific) placed at the hind paw of the mice. The changes exhibit an expected time lag relative to the changes in environmental oxygen concentration.

As a third example, continuous monitoring of calcium transients in neural tissues can yield essential insights into neural function and, therefore, into the causes of and treatments for mental disorders, including clinical depression, dementia, schizophrenia and autism[48,49]. A bioresorbable optical filter (such as that shown in Fig. 3a) integrated onto an Si nanomembrane-based bioresorbable photodetector (such as that shown in Fig. 1a) implanted into an animal model with a calcium-sensitive fluorescent dye (injected before implantation of the device; amount of injection: 2 μl) allows for measurements (Fig. 6h and Supplementary Fig. 15) that reflect neural activity. Figure 6h shows the photocurrent from a device implanted into the parietal lobe of a mouse, stained with small-molecule calcium fluorescent dyes

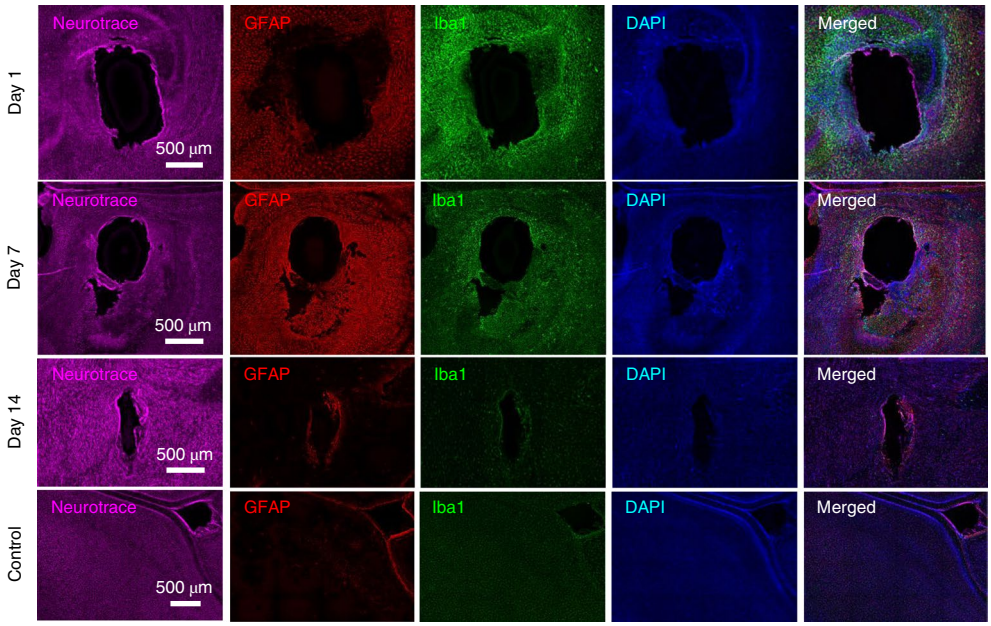

Fig. 7 | Representative confocal images of 30-μm horizontal striatal slices at various stages after implantation of the bioresorbable optical probes, compared with a control group. Probes were collected on days 1, 7 and 14, covering the typical lifetime of a bioresorbable device. The images show cross-sectional views of the implantation site with immunohistochemical staining for Nissl bodies (neurotrace, purple), astrocytes (glial fibrillary acidic protein (GFAP), red), activated microglia (Iba1, green) and DNA (4′,6-diamidino-2-phenylindole (DAPI), blue), and overall lesions from bioresorbable optical probes ($n = 3$ independent experiments).

(Oregon Green 488 BAPTA-2 AM). Anaesthesia using 1.7% isoflurane suppresses calcium transients, thereby resulting in the disappearance of spike events from in vivo measurements, consistent with existing literature, and confirming the expected operation of the device[50].

The three types of simple, bioresorbable photonic devices introduced here serve as enabling technologies for in vivo spectroscopic sensing. The components include Si nanomembrane photodetectors with wavelength-tunable light sources or with narrow-band optical filters, and tri-colour Si photodetectors with broad-band light. The small sizes of these systems minimize tissue disruption during implantation, and the biodegradability of the constituent materials leads to complete device clearance after a well-controlled operational time. Animal studies of the biodistribution of Si and Zn, the blood chemistry, and the haematology during and after the processes of bioresorption reveal no measurable toxic effects or immune responses. In vivo monitoring of cerebral temperature, cerebral oxygenation and neural activity in freely moving mice highlights some of the potential capabilities. These concepts establish unique approaches in biodegradable, or transient, photonic technologies with relevance to fundamental studies of disease pathology (such as cancer metastasis and neurological disorders) and neuroscience research, with additional possible utility in guiding surgical procedures and monitoring recovery from certain types of illness or injury.

Methods

Fabrication of the Si nanomembrane photodetector. Fabrication began with deposition of a 900-nm-thick layer of SiO_2 onto a silicon-on-insulator (SOI) substrate (thickness of Si device layer: 1,500 nm; Soitec) using PECVD. Photolithography and wet etching with buffered oxide etchant defined comb-like open areas for doping with boron (BN-1250; Saint-Gobain) at 1,000 °C for 30 min. The SiO_2 was completely removed by immersion in hydrofluoric acid solution (aqueous 49%) for 1 min. We followed similar procedures for phosphorus doping (PH-1000N; Saint-Gobain) as for boron doping (1,000 °C for 30 min). Unit cells of Si nanomembrane photodetectors were created by photolithography and reactive ion etching (SF_6 flow: 45 sccm; O_2 flow: 5 sccm; pressure: 30 mTorr; power: 150 W; 2.5 min). Immersion in hydrofluoric acid solution for 4 h fully undercut the buried oxide layer. A PDMS stamp allowed retrieval and delivery of these structures to a 10-μm-thick PLGA substrate at 60 °C on a hotplate, to complete the fabrication of the bioresorbable Si nanomembrane photodetectors. The PLGA substrate resulted from drop casting an ethyl acetate solution (7 wt%) on an Si substrate with a self-assembled monolayer formed using trimethoxymethylsilane.

Fabrication of the tri-colour photodetector. Fully formed Si NPNP junction layers fabricated on silicon-on-insulator wafers (thicknesses of NPNP junction layers: 200, 400, 1,400 and 4,500 nm, respectively; doping concentration: 10^{18} cm^{-3}; thickness of buried oxide layer: 3 μm) served as the source of bioresorbable active devices. Three consecutive processes of photolithography and reactive ion etching (SF_6 flow: 45 sccm; O_2 flow: 5 sccm; pressure: 30 mTorr; power: 150 W) opened contact areas for each junction layer. Another round of photolithography and reactive ion etching yielded isolated device unit cells. Immersion in hydrofluoric acid solution for 10 h fully undercut the buried oxide layer, thereby allowing the use of a PDMS stamp to retrieve and deliver the structures to a 10-μm-thick PLGA substrate at 60 °C on a hotplate to complete the fabrication.

Fabrication of the bioresorbable optical fibre. Fabrication began with melting PLGA (lactide:glycolide: 75:25; molecular weight: 66,000–107,000) in a small glass reservoir at 200 °C on a hotplate. Inserting a syringe needle with a diameter of 300 μm and slowly pulling it vertically yielded a PLGA fibre with a diameter of ~150 μm drawn from the reservoir. Dipping into sodium alginate solution (2 wt%) followed by immersion into a calcium chloride solution (0.5 wt%) formed a uniform cladding of bioresorbable hydrogel.

Fabrication of the bioresorbable optical filter. Alternating layers of SiO_x and SiN_y were deposited onto 100-μm-thick Si substrates using PECVD. PLGA drop cast from ethyl acetate solution (7 wt%) and baked at 70 °C, yielded a 10-μm-thick PLGA film attached to the multilayer. Etching under a vapour of xenon difluoride removed the Si handle substrate from the backside, thereby completing the fabrication.

Fabrication of the bioresorbable spectrometers. Fabrication began with lamination of a shadow mask made by laser milling on top of a bioresorbable photodetector (Si nanomembrane or tri-colour photodetector), followed by deposition of a 400-nm-thick film of Zn by electron beam evaporation to form Zn electrodes. The devices were completed by removing the shadow mask, sputtering a 50-nm-thick film of SiO_2, and aligning and attaching a bioresorbable optical filter on top at 65 °C on a hotplate.

Implantation of the bioresorbable spectrometer into the brains of live animals. All procedures associated with the animal studies followed the recommendations in the Guide for the Care and Use of Laboratory Animals of the National Institutes

of Health. The Institutional Animal Care and Use Committee at Northwestern University approved the protocol (protocol IS00005877). Female mice (CD-1; age at the initiation of the treatment: at least 6 weeks, but not more than 15 weeks; purchased from Charles River Laboratories) were acclimatized up to 5 d before surgery. Animals were anaesthetized using isoflurane gas (1–2%) during the implantation surgery. Craniotomy near the parietal lobe to the mice allowed the implantation of a bioresorbable spectrometer inside the cerebral region (Supplementary Fig. 13a). To monitor neural activity, injection of 2 µl Oregon Green (488 BAPTA-2 AM) in the parietal lobe was performed before implantation of the device. Applying dental cement (Fusio Liquid Dentin) and curing under ultraviolet light secured the implants. Mice were allowed to recover for 30 min before measurements.

Evaluation of the biodistribution, haematology and blood chemistry of mice. Overnight exposure to ultraviolet radiation sterilized the bioresorbable spectrometers, each of which consisted of an Si nanomembrane photodetector (length × width × thickness: 500 µm × 500 µm × 1,500 nm), two Zn electrodes (length × width × thickness: 10,000 µm × 200 µm × 400 nm) and a PLGA fibre (diameter: ~150 µm; length: 10,000 µm), before the implantation. The procedures involved anaesthetizing a female CD-1 mouse (Charles River Laboratories) with isoflurane gas (~2%), opening a 1-cm-length pocket at the subcutaneous region near the right flank, inserting the device into the pocket, and suturing to close the surgical opening. The procedures have been approved by the Institutional Animal Care and Use Committee of Northwestern University (protocol IS00005877). Daily checking, weighing and care of the mice ensured their moribund conditions and normal stress exposure. Euthanization of three mice at weeks 1, 3, 5 and 7 after device implantation enabled the extraction of blood, and explantation and weighing of organs, including the brain, heart, kidney, liver, lung, muscle and spleen. Charles River Laboratories conducted complete blood counts and blood chemistry tests on the blood samples collected in K-EDTA tubes and gel tubes, respectively. The explanted organs were split in half and stored in either pre-weighed 15-ml conical metal-free tubes in a −20 °C fridge or in 10% buffered formalin in 50-ml conical tubes, to prepare the tissue samples for biodistribution and histology studies, respectively. Tissues were dissolved by adding 1.5 ml nitric acid and 0.35 ml hydrogen peroxide to each tube. The tubes were kept in a water bath at 65 °C for 5 h. The dissolved tissue solutions were diluted 1:10 by adding Milli-Q water (MilliporeSigma), and analysed by ICP-OES and ICP-MS, yielding the concentrations of Si and Zn, respectively, in the tissues 1, 3, 5 and 7 weeks after implantation, to determine the biodistribution and biodegradability of dissolved Si and Zn.

Immunohistochemical analysis. Mice were given a lethal dose of pentobarbital sodium, followed by intracardial perfusion with 4% paraformaldehyde in PBS, as reported previously[51,52]. Then, the brains were dissected, post-fixed for 24 h at 4 °C, and cryoprotected with a solution of 30% sucrose in 0.1 M phosphate buffer (pH 7.4) at 4 °C for at least 24 h. This was followed by cutting into 30-µm sections, washing two or three times in PBS, and blocking in blocking buffer (PBS containing 0.5% Triton X-100 and 5% normal goat serum) for 1 h. Brain sections were then incubated for ~16 h at 4 °C in blocking buffer containing guinea pig anti-GFAP (1:500) and rabbit anti-Iba1 (1:300). After the incubation, sections were washed three times in PBS and then incubated for 2 h at room temperature in blocking buffer containing Alexa Fluor 488 goat anti-rabbit IgG (1:1,000), Alexa Fluor 568 goat anti-guinea pig IgG (1:1,000) and Neurotrace 435/455 Blue Fluorescent Nissl stain (1:100). Following the secondary antibody, sections were washed three times in PBS followed by three washes in phosphate buffer, and then mounted on glass slides with hardset Vectashield (Vector Laboratories). A Leica SP8 confocal microscope enabled imaging of all of the sections, with gain, exposure time and z-stack size remaining constant throughout each experiment. All images were processed with the same settings using the Fiji software by ImageJ.

Reporting Summary. Further information on research design is available in the Nature Research Reporting Summary linked to this article.

Data availability

The main data supporting the results of this study are available within the paper and its Supplementary Information files. The raw and analysed datasets generated during the study are available for research purposes from the corresponding author on reasonable request.

Received: 3 October 2018; Accepted: 3 July 2019;
Published online: 7 August 2019

References

1. Hotamisligil, G. S. Inflammation and metabolic disorders. *Nature* **444**, 860–867 (2006).
2. Lo, E. H., Dalkara, T. & Moskowitz, M. A. Mechanisms, challenges and opportunities in stroke. *Nat. Rev. Neurosci.* **4**, 399–414 (2003).
3. DeBerardinis, R. J. & Chandel, N. S. Fundamentals of cancer metabolism. *Sci. Adv.* **2**, e1600200 (2016).
4. Tai, L.-C. et al. Methylxanthine drug monitoring with wearable sweat sensors. *Adv. Mater.* **30**, 1707442 (2018).
5. Kim, H. et al. Single-neuronal cell culture and monitoring platform using a fully transparent microfluidic DEP device. *Sci. Rep.* **8**, 13194 (2018).
6. Bettinger, C. J. Recent advances in materials and flexible electronics for peripheral nerve interfaces. *Bioelectron. Med.* **4**, 6 (2018).
7. Hamaoka, T., McCully, K. K., Niwayama, M. & Chance, B. The use of muscle near-infrared spectroscopy in sport, health and medical sciences: recent developments. *Phil. Trans. R. Soc. A Math. Phys. Eng. Sci.* **369**, 4591–4604 (2011).
8. Ferrari, M. & Quaresima, V. A brief review on the history of human functional near-infrared spectroscopy (fNIRS) development and fields of application. *Neuroimage* **63**, 921–935 (2012).
9. Lloyd-Fox, S., Blasi, A. & Elwell, C. E. Illuminating the developing brain: the past, present and future of functional near infrared spectroscopy. *Neurosci. Biobehav. Rev.* **34**, 269–284 (2010).
10. Hwang, S.-W. et al. A physically transient form of silicon electronics. *Science* **337**, 1640–1644 (2012).
11. Kang, S. et al. Bioresorbable silicon electronic sensors for the brain. *Nature* **530**, 71–76 (2016).
12. Tao, H. et al. Silk-based resorbable electronic devices for remotely controlled therapy and in vivo infection abatement. *Proc. Natl Acad. Sci. USA* **111**, 17385–17389 (2014).
13. Luo, M., Martinez, A. W., Song, C., Herrault, F. & Allen, M. G. A microfabricated wireless RF pressure sensor made completely of biodegradable materials. *J. Micro. Syst.* **23**, 4–13 (2014).
14. Lu, L. et al. Biodegradable monocrystalline silicon photovoltaic microcells as power supplies for transient biomedical implants. *Adv. Energy Mater.* **8**, 1703035 (2018).
15. Bai, W. et al. Flexible transient optical waveguides and surface-wave biosensors constructed from monocrystalline silicon. *Adv. Mater.* **30**, 1801584 (2018).
16. Nizamoglu, S. et al. Bioabsorbable polymer optical waveguides for deep-tissue photomedicine. *Nat. Commun.* **7**, 10374 (2016).
17. Yu, K. J. et al. Bioresorbable silicon electronics for transient spatiotemporal mapping of electrical activity from the cerebral cortex. *Nat. Mater.* **15**, 782–791 (2016).
18. Fang, H. et al. Capacitively coupled arrays of multiplexed flexible silicon transistors for long-term cardiac electrophysiology. *Nat. Biomed. Eng.* **1**, 0038 (2017).
19. Son, D. et al. Bioresorbable electronic stent integrated with therapeutic nanoparticles for endovascular diseases. *ACS Nano* **9**, 5937–5946 (2015).
20. Karliczek, A. et al. Intraoperative assessment of microperfusion with visible light spectroscopy for prediction of anastomotic leakage in colorectal anastomoses. *Color. Dis.* **12**, 1018–1025 (2010).
21. Bogomolov, A. et al. Development and testing of an LED-based near-infrared sensor for human kidney tumor diagnostics. *Sensors* **17**, 1914 (2017).
22. Yun, S. H. & Kwok, S. J. J. Light in diagnosis, therapy and surgery. *Nat. Biomed. Eng.* **1**, 0008 (2017).
23. Du, Q. et al. Chip-scale broadband spectroscopic chemical sensing using an integrated supercontinuum source in a chalcogenide glass waveguide. *Photonics Res.* **6**, 506–510 (2018).
24. Warden, M. R., Cardin, J. A. & Deisseroth, K. Optical neural interfaces. *Annu. Rev. Biomed. Eng.* **16**, 103–129 (2014).
25. Kang, S.-K. et al. Dissolution behaviors and applications of silicon oxides and nitrides in transient electronics. *Adv. Funct. Mater.* **24**, 4427–4434 (2014).
26. Fu, R. et al. Implantable and biodegradable poly(L-lactic acid) fibers for optical neural interfaces. *Adv. Opt. Mater.* **6**, 1700941 (2018).
27. Lee, Y. K. et al. Dissolution of monocrystalline silicon nanomembranes and their use as encapsulation layers and electrical interfaces in water-soluble electronics. *ACS Nano* **11**, 12562–12572 (2017).
28. Yin, L. et al. Dissolvable metals for transient electronics. *Adv. Funct. Mater.* **24**, 645–658 (2014).
29. Yin, L. et al. Mechanisms for hydrolysis of silicon nanomembranes as used in bioresorbable electronics. *Adv. Mater.* **27**, 1857–1864 (2015).
30. Kang, S. K. et al. Dissolution chemistry and biocompatibility of silicon- and germanium-based semiconductors for transient electronics. *ACS Appl. Mater. Interfaces* **7**, 9297–9305 (2015).
31. Brown, J. Q., Vishwanath, K., Palmer, G. M. & Ramanujam, N. Advances in quantitative UV-visible spectroscopy for clinical and pre-clinical application in cancer. *Curr. Opin. Biotechnol.* **20**, 119–131 (2009).
32. Menon, L. et al. Transferred flexible three-color silicon membrane photodetector arrays. *IEEE Photonics J.* **7**, 1–6 (2015).
33. Liu, C. et al. High performance, biocompatible dielectric thin-film optical filters integrated with flexible substrates and microscale optoelectronic devices. *Adv. Opt. Mater.* **6**, 1800146 (2018).
34. Macleod, H. A. & Hugh, A. *Thin-Film Optical Filters* (CRC Press/Taylor & Francis, 2010).

35. Chen, T.-W. et al. Ultrasensitive fluorescent proteins for imaging neuronal activity. *Nature* **499**, 295–300 (2013).
36. Besser, R. S., Louris, P. J. & Musket, R. G. Chemical etch rate of plasma-enhanced chemical vapor deposited SiO_2 films. *J. Electrochem. Soc.* **144**, 2859–2864 (1997).
37. Kraitl, J., Timm, U. & Ewald, H. Non-invasive measurement of blood and tissue parameters based on VIS-NIR spectroscopy. In *Proc. SPIE* 8591 (SPIE, 2013).
38. Lu, G. & Fei, B. Medical hyperspectral imaging: a review. *J. Biomed. Opt.* **19**, 010901 (2014).
39. Ciurczak, E. W. & Igne, B. *Pharmaceutical and Medical Applications of Near-Infrared Spectroscopy* 2nd edn (CRC Press, 2014).
40. Durduran, T., Choe, R., Baker, W. B. & Yodh, A. G. Diffuse optics for tissue monitoring and tomography. *Rep. Prog. Phys.* **73**, 076701 (2010).
41. Mrozek, S., Vardon, F. & Geeraerts, T. Brain temperature: physiology and pathophysiology after brain injury. *Anesthesiol. Res. Pract.* **2012**, 989487 (2012).
42. Wang, H. et al. Brain temperature and its fundamental properties: a review for clinical neuroscientists. *Front. Neurosci.* **8**, 307 (2014).
43. Ho, C. L., Wang, C. M., Lee, K. K., Ng, I. & Ang, B. T. Cerebral oxygenation, vascular reactivity, and neurochemistry following decompressive craniectomy for severe traumatic brain injury. *J. Neurosurg.* **108**, 943–949 (2008).
44. Leal-Noval, S. R. et al. Invasive and noninvasive assessment of cerebral oxygenation in patients with severe traumatic brain injury. *Intensive Care Med.* **36**, 1309–1317 (2010).
45. Toet, M. C., Lemmers, P. M. A., van Schelven, L. J. & van Bel, F. Cerebral oxygenation and electrical activity after birth asphyxia: their relation to outcome. *Pediatrics* **117**, 333–339 (2006).
46. Brassard, P., Ainslie, P. N. & Secher, N. H. Cerebral oxygenation in health and disease. *Front. Physiol.* **5**, 458 (2014).
47. Van Bel, F. & Mintzer, J. P. Monitoring cerebral oxygenation of the immature brain: a neuroprotective strategy? *Pediatr. Res.* **84**, 159–164 (2018).
48. Tye, K. M. & Deisseroth, K. Optogenetic investigation of neural circuits underlying brain disease in animal models. *Nat. Rev. Neurosci.* **13**, 251–266 (2012).
49. Cui, G. et al. Concurrent activation of striatal direct and indirect pathways during action initiation. *Nature* **494**, 238–242 (2013).
50. Thrane, A. S. et al. General anesthesia selectively disrupts astrocyte calcium signaling in the awake mouse cortex. *Proc. Natl Acad. Sci. USA* **109**, 18974–18979 (2012).
51. Siuda, E. R., Al-Hasani, R., McCall, J. G., Bhatti, D. L. & Bruchas, M. R. Chemogenetic and optogenetic activation of Gαs signaling in the basolateral amygdala induces acute and social anxiety-like states. *Neuropsychopharmacology* **41**, 2011–2023 (2016).
52. Jeong, J.-W. et al. Wireless optofluidic systems for programmable in vivo pharmacology and optogenetics. *Cell* **162**, 662–674 (2015).

Acknowledgements

W.Z. acknowledges support from the Army Research Office under grant W911NF-15-1-0035. This work utilized the Northwestern University Micro/Nano Fabrication Facility, which is partially supported by the Soft and Hybrid Nanotechnology Experimental Resource (NSF ECCS-1542205), Materials Research Science and Engineering Center (NSF DMR-1121262), State of Illinois, Northwestern University and Center for Bio-Integrated Electronics (Simpson Querrey Institute). The Center for Developmental Therapeutics is supported by Cancer Center Support Grant P30 CA060553 from the National Cancer Institute, awarded to the Robert H. Lurie Comprehensive Cancer Center.

Author contributions

W.B., R.F., J.S., D.L., X.N., Y.P., Z.L., T.H., Y.L., D.W., H.Z., X.S., L.Y., W.Z. and J.A.R. designed and fabricated the devices, and performed the analysis. W.B., I.K., J.S., D.L., X.N., Y.P., I.S. and F.A. performed the animal study. C.R.H. and A.B. performed the computed tomography imaging. W.B., I.K, J.S., D.W., X.N., Q.Y., J.Z., K.M. and M.P. performed the study of bioresorption, biodistribution and toxicity. W.B., J.S., I.K., R.F., W.Z. and J.A.R wrote the manuscript with input from all authors.

Competing interests

The authors declare no competing interests.

Additional information

Supplementary information is available for this paper at https://doi.org/10.1038/s41551-019-0435-y.

Reprints and permissions information is available at www.nature.com/reprints.

Correspondence and requests for materials should be addressed to J.A.R.

Publisher's note: Springer Nature remains neutral with regard to jurisdictional claims in published maps and institutional affiliations.

nature research

Corresponding author(s): John A. Rogers

Last updated by author(s): Jun 22, 2019

Reporting Summary

Nature Research wishes to improve the reproducibility of the work that we publish. This form provides structure for consistency and transparency in reporting. For further information on Nature Research policies, see Authors & Referees and the Editorial Policy Checklist.

Statistics

For all statistical analyses, confirm that the following items are present in the figure legend, table legend, main text, or Methods section.

n/a	Confirmed	
☐	☒	The exact sample size (*n*) for each experimental group/condition, given as a discrete number and unit of measurement
☐	☒	A statement on whether measurements were taken from distinct samples or whether the same sample was measured repeatedly
☒	☐	The statistical test(s) used AND whether they are one- or two-sided *Only common tests should be described solely by name; describe more complex techniques in the Methods section.*
☐	☒	A description of all covariates tested
☒	☐	A description of any assumptions or corrections, such as tests of normality and adjustment for multiple comparisons
☐	☒	A full description of the statistical parameters including central tendency (e.g. means) or other basic estimates (e.g. regression coefficient) AND variation (e.g. standard deviation) or associated estimates of uncertainty (e.g. confidence intervals)
☒	☐	For null hypothesis testing, the test statistic (e.g. *F*, *t*, *r*) with confidence intervals, effect sizes, degrees of freedom and *P* value noted *Give P values as exact values whenever suitable.*
☒	☐	For Bayesian analysis, information on the choice of priors and Markov chain Monte Carlo settings
☒	☐	For hierarchical and complex designs, identification of the appropriate level for tests and full reporting of outcomes
☒	☐	Estimates of effect sizes (e.g. Cohen's *d*, Pearson's *r*), indicating how they were calculated

Our web collection on statistics for biologists contains articles on many of the points above.

Software and code

Policy information about availability of computer code

Data collection	Fig. 1f,g, Fig. 2e, Fig. 5a,e,g,h, and Fig. 6e,h used LabVIEW SignalExpress for DMM (2013) software, available for download online (model USB-4065) from National Instruments. Fig. 2f,g, Fig. 5c and Fig. 6f used Agilent BenchLink Data Logger 3, 2012-01-01, version 4.3.00, available online from Keysight Technology. Fig. 1e,h and Fig. 2d used EasyEXPERT group+ Device Characterization Software, version 2013, from Keysight Technology. Fig. 3e,f,g used UV WinLab Software for Uv/Vis software, from PerkinElmer Inc. Fig. 6e, thermal images, were analyzed by FLIR Tools+ software, from FLIR Systems, Inc.
Data analysis	Microsoft Excel and OriginPro 9.1 were used for data analysis and plotting. The immunohistochemistry was analyzed by Fiji Imagej.

For manuscripts utilizing custom algorithms or software that are central to the research but not yet described in published literature, software must be made available to editors/reviewers. We strongly encourage code deposition in a community repository (e.g. GitHub). See the Nature Research guidelines for submitting code & software for further information.

Data

Policy information about availability of data

All manuscripts must include a data availability statement. This statement should provide the following information, where applicable:

- Accession codes, unique identifiers, or web links for publicly available datasets
- A list of figures that have associated raw data
- A description of any restrictions on data availability

The authors declare that the main data supporting the results in this study are available within the paper and its Supplementary Information. The raw and analysed datasets generated during the study are available for research purposes from the corresponding author on reasonable request.

Field-specific reporting

Please select the one below that is the best fit for your research. If you are not sure, read the appropriate sections before making your selection.

☒ Life sciences ☐ Behavioural & social sciences ☐ Ecological, evolutionary & environmental sciences

For a reference copy of the document with all sections, see nature.com/documents/nr-reporting-summary-flat.pdf

Life sciences study design

All studies must disclose on these points even when the disclosure is negative.

Sample size	The work was explorative; therefore, we did not estimate the sample size needed. We used a sample size of 6 for characterizing responses of the bioresorbable spectrometer (Fig. 1e-h, Fig. 2, and Supplementary Figs 1, 3, 4a-c, 6, 20 and 22). We used 3 biologically independent mice for characterizing the in vivo bioresorption of the devices (Fig. 1i, Supplementary Figs 4d, 9 and 19). We used a sample size of 3 for the optical properties and bioresorbable property of the multilayer optical filter (Fig. 3, Supplementary Figs 7, 16, 24 and 25). A total sample size of 12 was used to study the elemental biodistribution and biocompatibility of the bioresorbable devices (Fig. 4a,b,d,e, and Supplementary Fig. 8). A sample size of 3 was used for in vitro demonstration of the bioresorbable devices (Fig. 5, and Supplementary Figs 10, 11, 12 and 21). A sample size of 4 was used in the monitoring of intracranial oxygenation, temperature, and neural activity by implantation of the bioresorbable optical probes (Fig. 6, and Supplementary Figs 14 and 15).
Data exclusions	No data were excluded from the analyses.
Replication	The in vitro and in vivo pressure measurements, and the in vitro dissolution studies, were carried out more than 3 times to ensure replicability. The results were consistent and replicable.
Randomization	All devices and animals tested were selected randomly.
Blinding	No blinding was necessary as there were no significant variations in the animals tested.

Reporting for specific materials, systems and methods

We require information from authors about some types of materials, experimental systems and methods used in many studies. Here, indicate whether each material, system or method listed is relevant to your study. If you are not sure if a list item applies to your research, read the appropriate section before selecting a response.

Materials & experimental systems

n/a	Involved in the study
☐	☒ Antibodies
☒	☐ Eukaryotic cell lines
☒	☐ Palaeontology
☐	☒ Animals and other organisms
☒	☐ Human research participants
☒	☐ Clinical data

Methods

n/a	Involved in the study
☒	☐ ChIP-seq
☒	☐ Flow cytometry
☒	☐ MRI-based neuroimaging

Antibodies

Antibodies used	Goat anti-Rabbit IgG (H+L) Cross-Adsorbed Secondary Antibody, Alexa Fluor 488, ThermoFisher Scientific, # A-11008 Goat anti-Mouse IgG (H+L) Cross-Adsorbed Secondary Antibody, Alexa Fluor 568, ThermoFisher Scientific, # A-11004 GFAP Polyclonal Antibody, ThermoFisher Scientific, # PA5-16291 IBA1 Polyclonal Antibody, ThermoFisher Scientific, # PA5-27436
Validation	W. Liu, et al, Front. Immunol., 13 February 2018 | https://doi.org/10.3389/fimmu.2018.00223 A. Schober, et al, Front. Cell. Neurosci., 11 November 2016 | https://doi.org/10.3389/fncel.2016.00262 J. Gray, et al, Molecular Psychiatry volume 23, pages 904–913 (2018) V. Ozacmak, et al, Nutr Neurosci. 2016 May;19(4):176-86. doi: 10.1179/1476830515Y.0000000027.

Animals and other organisms

Policy information about studies involving animals; ARRIVE guidelines recommended for reporting animal research

Laboratory animals	Female CD-1 mice from Charles River weighing 20–25 grams, 6–15 weeks old at the time of implant.
Wild animals	The study did not involve wild animals.
Field-collected samples	The study did not involve samples collected from the field.
Ethics oversight	All procedures associated with animal studies followed recommendations in the Guide for the Care and Use of Laboratory Animals of the National Institute of Health. The Institutional Animal Care and Use Committee (IACUC) at Northwestern University approved the protocol (protocol IS00005877).

Note that full information on the approval of the study protocol must also be provided in the manuscript.